Emerging proton conductivity at the interface between insulating $NdGaO_3$ and $BaZrO_3$

Francesca Zarotti,[1,2] Roberto Felici,[2] Vittorio Foglietti,[2] Zhao Liu,[3] Nan Yang,[3] and Giuseppe Balestrino[1,2]
[1]*DICII, Università di Roma Tor Vergata, Via del Politecnico 1, I-00133 Roma, Italy*
[2]*CNR-SPIN, Sede di Tor Vergata, DICII, Via del Politecnico 1, I-00133 Roma, Italy*
[3]*School of Physical Science and Technology, ShanghaiTech University, Shanghai, People's Republic of China*

(Received 7 June 2019; published 24 October 2019)

This article reports on the interplay between structural properties of the interface region and emerging proton conductivity in thin films of insulating $BaZrO_3$ perovskite deposited by pulsed laser ablation onto $NdGaO_3$ wide-band-gap insulators. High-resolution transmission electron microscopy and surface x-ray diffraction reveal the presence of a large number of misfit dislocations at the interface, allowing the full relaxation of the epitaxial strain. An analysis of the x-ray diffraction patterns reveals strain relaxation that occurs over a thickness of about 3 nm, equally divided between the film and the substrate. Electrical impedance spectroscopy measurements show a sizeable proton conductance that can mainly be attributed to the defective interface. Assuming that proton conduction occurs in the interface layer, values of interface conductivity of about 0.5 S/cm at 650 °C are estimated with an activation energy of about 0.86 eV. Experimental findings are explained assuming that the defective interface layer can accommodate a very large concentration of carriers whose mobility is somewhat hindered by the high concentration of structural defects at the interface.

DOI: 10.1103/PhysRevMaterials.3.103606

I. INTRODUCTION

A large variety of novel physical and chemical properties can arise at the interface between different oxides stacked in a single heteroepitaxial structure [1]. A short list of such properties includes high-mobility two-dimensional (2D) electron gas [2], 2D superconductivity [3–5], and orbital and magnetic reconstruction [6]. Moreover, in addition to the electronic properties, ionic properties of interfaces between oxides currently attract an increasing interest: in some cases, a sizeable increase of the ionic/proton conduction, up to a few orders of magnitude, was observed in superlattices where a large number of layers were stacked in a sequence [7]. Such novel properties were attributed to different interface phenomena that include epitaxial strain, occurrence of a regular network of interface dislocations [8–10], the presence of space-charge regions induced by cation redistribution, and interface selective doping (see, for instance, Guo and Maier [11] for a review concerning halides and oxides).

In this framework, Sata *et al.* [12] investigated CaF_2/BaF_2 superlattices consisting of thin individual layers (a few tens of nanometers) and observed an increase of about 2 orders of magnitude in the overall in-plane ionic conductivity when the individual thickness of the layers was reduced to about 20 nm. This effect was attributed to space-charge effects with consequent accumulation of F^- carriers at the interface. Ionic conduction was also investigated in YSZ/R_2O_3 heterostructures [13,14] (YSZ denotes Y-doped ZrO_2, while R_2O_3 refers to Lu_2O_3, Y_2O_3, and Sc_2O_3, respectively). Three systems were investigated: YSZ/Lu_2O_3 with almost zero mismatch (i.e., close to coherent interface), YSZ/Y_2O_3 with a significant tensile stress, and YSZ/Sc_2O_3 films with a significant compressive stress. In this case, the authors concluded that the variation of the ionic conductivity could be attributed to a change in the vacancy's mobility caused by the elastic strain rather than by a change in the carrier concentration. Similarly, superlattices based on Sm-doped ceria and yttrium-stabilized zirconia layers showed a significant increase of the ionic conductivity [15]. Once more, tensile strain effects were suggested to be at the origin of the observed conductivity enhancement. More recently, the role of the network of misfit dislocations in the proton conduction of the interface between neodymium gallate and yttrium-doped barium zirconate was investigated [16–18]. Surface x-ray diffraction (SXRD) measurements carried out on this system showed that the strain field related to the network of dislocations at the interface depends on the annealing conditions, being larger in the case of annealing in wet conditions as compared to annealing in dry atmosphere. This result supports the role of the dislocations cores as a reservoir for hydroxyl groups.

The whole set of studies quoted above indicates that heterointerfaces and superlattices based on materials with different lattice parameters represent a promising field both for studying some fundamental aspects of ionic conduction and for applications like fuel cells and surface catalysis or water splitting [19]. However, some critical issues concerning interfaces and superlattices must be considered before drawing firm conclusions about ionic/proton conduction. Most of the heterostructures considered above are highly mismatched, namely, the constituent oxides have a different crystallographic structure and/or quite different lattice parameter values. This usually results in a fast relaxation of the mismatch, through structural defects, leading to a loss of the structural coherence, in the direction perpendicular to the interface, within a few crystallographic unit cells (u.c.). Therefore, transport properties in superlattices, made of a large number of interfaces stacked in a sequence, can vary strongly along the multilayer because of the progressive degradation of the

structural quality as the distance from the substrate increases. In superlattices the transport properties should then be determined as a function of the distance from the substrate with a spatial resolution high enough to highlight the role of the interfaces. In order to understand the cause of this increase in conductivity, the transport properties of the interface between an ordered substrate and a single overlayer have to be determined accurately. This procedure has been applied for understanding the "electronic" properties of individual interfaces that present electronic features qualitatively different from those of the constituent layers (i.e., 2D electron gas [2] or 2D superconductivity [5]). The same approach is more critical when applied to the study of the ionic/protonic conduction of an interface. In the latter case the expected changes in the conductance can be quite small in comparison with the contributions from the substrate and the film.

In the present paper, we investigate the conduction properties of a single interface between a $NdGaO_3$ (NGO) substrate and a $BaZrO_3$ (BZO) film. The two compounds have both a cubic perovskite structure (actually pseudocubic in the case of $NdGaO_3$, see Supplemental Material (SM) [20] and Fig. 1 of [18] for a discussion about the true structure), but with a large difference in the value of the cubic lattice parameter (0.424 nm for $BaZrO_3$ [21] vs 0.386 nm for $NdGaO_3$ [22]). Both compounds are undoped and, consequently, they are expected to be insulators, either electronic or ionic. On the contrary, electric measurements show a sizeable conductance, particularly high in wet atmosphere, because of the interaction between the two constituent layers. A careful investigation of the structural properties of the interface through high-resolution transmission electron microscopy (HRTEM), x-ray reflectivity (XRR), and SXRD allowed relating the transport properties with a defective layer at the interface between the two compounds whose thickness is in the nanometric range.

II. EXPERIMENTAL

BZO films were deposited on $5 \times 5\,mm^2$ NGO [(110)-oriented] substrates by the pulsed laser deposition (PLD) technique. NGO was chosen as substrate for its relatively wide band gap and low electronic conductivity. BZO targets were prepared using a powder synthesized by solid-state reaction. Starting materials of $BaCO_3$ (99.9%, Sigma-Aldrich), and ZrO_2 (99.9%, Sigma-Aldrich) were mixed with distilled water, and then a ball miller was used at a speed of 300 rpm for 12 h. After milling and drying, powders were calcined at 1450 °C in air for 8 h. During the heating and cooling processes, samples were heated or cooled to the desired temperature at a rate of 7 °C/min in order to obtain the BZO perovskite compound. The PLD apparatus is based on the use of a KrF excimer pulsed laser source (Compex Pro 110 F, $\lambda = 248$ nm) operated at 10 Hz with an energy density of $2.25\,J/cm^2$. The growth temperature was held at a value of about 800 °C, while the O_2 pressure in the chamber was 5 Pa with a constant O_2 flux of 50 sccm. The thermal contact between the sample holder and the substrate was provided by Ag paste. The target-to-substrate distance was kept at 60 mm. BZO films with different thicknesses, ranging from 2.5 to 500 nm, were deposited under the same growth conditions.

The HRTEM analysis was performed by JEM-2100Plus multipurpose transmission electron microscope, combining the optics of the original JEM-2100 with an advanced control system for enhanced ease of operation.

The x-ray data were collected at the ID03 SXRD beamline of the European Synchrotron Radiation Facility, ESRF, in Grenoble, France [23]. The incident beam was fixed at an energy value of 16.5 keV, and it was focused at the sample position to be $100 \times 50\,\mu m^2$ in the directions parallel and perpendicular to the sample surface, respectively. A 2×2 2D Maxipix detector was used for the experiment. Each pixel of the detector was treated as an independent detector, and the diffracted intensity was then projected in the reciprocal space by using the BINOCULARS software [24].

XRR measurements were carried out at the SixS (Surface Interface X-ray Scattering) beamline of the SOLEIL synchrotron facility in Paris, France, by using monochromatic x rays of 15-keV photon energy [25]. Specular rods were examined using WINROD software [26,27].

Electrochemical impedance spectroscopy (EIS) [28] measurements, performed in order to study the transport properties of the films, were carried out using a frequency response analyzer coupled with a dielectric interface. Impedance was measured in dry air and in wet H_2 atmospheres in the temperature range between 400 °C and 650 °C. The frequency range was 5 MHz–10 mHz with an amplitude AC voltage of 100 mV. Two in-plane blocking platinum electrodes, $2 \times 5\,mm^2$, were used for the impedance characterization; therefore, EIS measurements exclusively probe the longitudinal, in-plane conductivity.

III. RESULTS AND DISCUSSION

Figure 1 shows the high-resolution TEM image of the interface between the NGO substrate and the BZO film. In order to obtain the HRTEM image, a 100-nm-thick BZO sample was cut along the [110] in-plane pseudocubic crystallographic direction (a definition of the pseudocubic lattice is given in Ref. [18]). Therefore, in Fig. 1, the interface between the film and the substrate runs parallel to the [110] pseudocubic direction, while the growth direction (perpendicular to the interface) corresponds to the [001] pseudocubic direction. A large number of misfit dislocations appears at the interface in order to relax the large lattice mismatch (about 9%) between the pseudocubic lattice parameters of the substrate and the cubic lattice parameters of the film; the yellow arrows in panel (a) indicate individual dislocations. Dislocations are confined in a narrow interface layer [see panel (b)]. For a fully relaxed structure the expected periodicity Λ of the misfit dislocations (MDs) network at the interface is given by [18]

$$\Lambda = \frac{a_{BZO} \times a_{NGO}}{a_{BZO} - a_{NGO}} \cong 4.8\ \text{nm}. \quad (1)$$

Furthermore, panel (a) shows that the interface MD network is quite disordered, namely, the distance between neighbor dislocations (Λ^*) strongly fluctuates along the interface. In the inset of panel (a), yellow diamonds represent the experimental Λ^* values along the [110] direction. The red curve represents the Gaussian fit of the experimental Λ^* values distribution. The distribution is peaked at about 3 nm and it

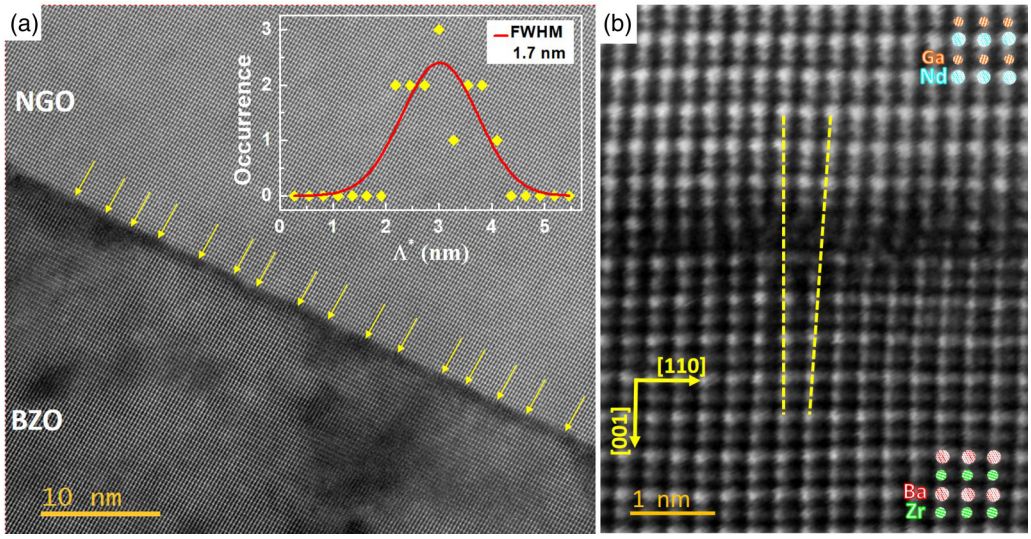

FIG. 1. High-resolution TEM image of the BZO/NGO interface. The imaged surface is along the (110) plane of the pseudocubic cell of the NGO. In (a) each yellow arrow indicates a dislocation at the interface. The inset of panel (a) shows the distribution of the distance between two adjacent dislocations in nanometers. The red curve represents the Gaussian fit of the dislocation distribution, peaked at about 3 nm with a FWHM value of about 1.7 nm. In (b) a zoom-in of the interface region is shown. The crystallographic orientation of the BZO cross-section plane and the relative position of Ba and Zr atoms are reported. Relative positions of Nd and Ga cations of NGO substrate are also displayed. Yellow dotted lines represent the linear strain relaxation according to the model displayed in Fig. 2.

has a FWHM of about 1.7 nm. In order to relate the latter quantity to the expected theoretical Λ value of Eq. (1), we have to keep in mind that the HRTEM image represents the $(-1\ 1\ 0)$ plane of the cubic structures. On the other hand, as shown by x-ray diffraction measurements reported in the SM [20], the dislocations run along the main crystallographic pseudocubic directions, i.e., along the [100] and [010] directions. Therefore, in order to make a direct comparison between the experimental Λ^* values and the expected spacing according to Eq. (1), we have to correct Λ^* by a geometrical factor $2/\sqrt{2}$. This leads to an experimental Λ value of 4.2 nm with a large dispersion of about 2.4 nm, in good agreement with the value given by Eq. (1). In panel (b) a zoom of the interface region centered at a misfit dislocation is shown. For sake of clarity, we have indicated the crystallographic orientations of the BZO cross-section plane and the position of the two cations: red circles indicate Ba ions, while green circles indicate Zr ions. Yellow dotted lines are a guide for the eye, assuming a linear strain relaxation.

Figure 2 shows a small portion of the interface simulated according to a crude model of strain relaxation based on the indications of the HRTEM images and the SXRD maps. Far from the interface, on both sides (substrate and film), the lattice parameter assumes the bulk value (of NGO and BZO, respectively). At the interface, a disordered network of dislocations is simulated with missing rows of BZO separated by a distance Λ. Λ values fluctuate with a Gaussian distribution having a FWHM of 6 u.c., in agreement with the inset of Fig. 1(a). The lattice spacing increases linearly, starting from the bulk value of NGO, both in the substrate (along 4 u.c.) and in the film (along 4 u.c.), until it reaches the bulk value of BZO. Dashed lines in the figure are a guide for the eye, illustrating the strain relaxation. The overall thickness of the strained interface region is 8 u.c., corresponding to about 3 nm.

The interface properties were also investigated by XRR and SXRD using synchrotron radiation. Figure 3 shows the (001) reflection of the thinnest 2.9-nm-thick BZO film grown on a NGO substrate. The strong peak at $L = 1$ is associated with the NGO substrate. The shoulder on the left side of the substrate peak and the intensity oscillations on both sides are the result of the interference between substrate and BZO film [29]. Data were simulated by a BZO film

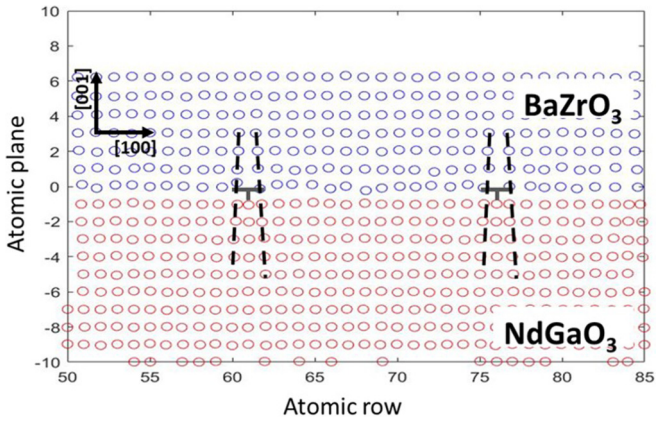

FIG. 2. Schematic model of strain relaxation at the interface. The interface plane is located at the zero reference point. Blue circles and red circles represent the atom positions in BZO and NGO structures, respectively. The mean distance between dislocations and their variance is fixed according to the results in the inset of Fig. 1(a). The strain is supposed to relax linearly symmetrically in the substrate (4 u.c.) and in the film (4 u.c.). The overall thickness of the interface region is 8 u.c., corresponding to about 3 nm.

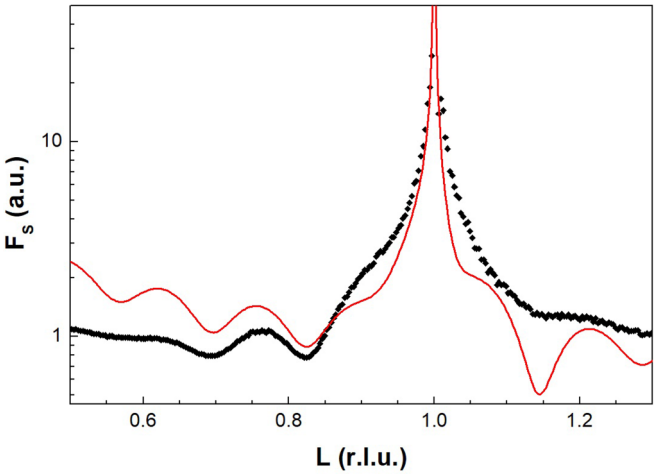

FIG. 3. (001) specular rod of 2.9-nm-thick BZO. The red line represents the simulation of the interference between the NGO substrate and thin BZO film. The total thickness of the film is 7 u.c., with a value of lattice parameter c_{BZO} of about 0.42 nm.

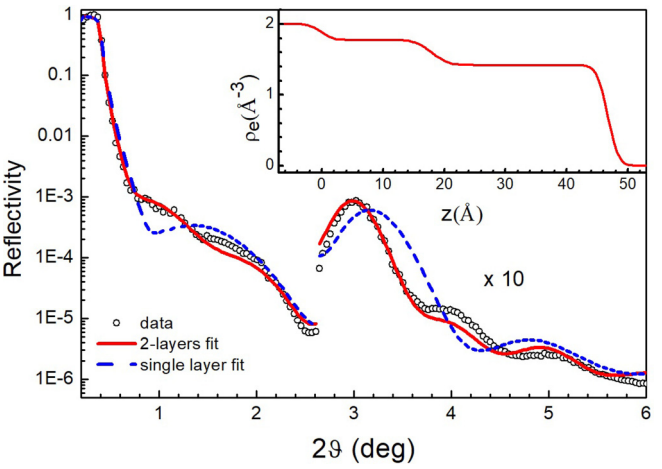

FIG. 4. Reflectivity plot of a 2.9-nm-thick BZO film. In the main panel two different theoretical simulations are compared with the experimental data. The blue dashed line refers to a simulation of a single-layer 2.9-nm-thick (∼7 u.c.) BZO film on the NGO substrate. The red full line is the best fit obtained adding an interface layer between the substrate and the film, 1.8 nm (∼4 u.c.). In the inset the electronic density profile of the sample as a function of distance z from the substrate is reported. Fit parameters referring to the two-layer simulation are listed in Table I of the Supplemental Material [20].

consisting of 7 u.c. Moreover, two parameters (d_1, d_2), one (d_1) counting for the distance between the outmost plane NdO of NGO and first plane ZrO_2 of BZO and one (d_2) counting for the expansion/compression of the BZO cell along the z direction, have been introduced. The best simulation, red curve in Fig. 3, is obtained assuming the film lattice parameter c_{BZO} equal to 0.42 nm and a distance d_1 slightly larger than $c_{BZO}/2$(∼0.213 nm). Although the simulation is very crude and does not take into account any effect related to distortion of the structure or to thermal disorder (Debye-Waller factors), it reproduces the features of the experimental pattern: (a) peaks positions [$L \approx 0.63, 0.77, 1.22$ reciprocal lattice unit (r.l.u.)], (b) minima at $L \approx 0.7$, 0.83, 1.15 r.l.u., and (c) the presence of a shoulder at $L \approx 0.9$ r.l.u.

Figure 4 shows the reflectivity plot of the 2.9-nm-thick BZO film: in the main panel we report, together with the reflectivity experimental data (empty dots), two different theoretical simulations of the experimental behavior. The blue dashed line represents the simulation with a single interface and a single homogeneous layer. The theoretical curve roughly reproduces the leading oscillations of the experimental curve but definitely fails in reproducing the beats in the angular range between 3 and 5 degrees. In order to better simulate the experimental data in the full angular range investigated, it is necessary to add a second layer at the interface with an electronic density intermediate between NGO and BZO. The red full line represents the double-layer simulation. The inset of Fig. 4 shows the electronic density profile for the two-layer simulation. The interface layer is about 1.8-nm-thick, while the upmost layer is about 2.9 nm thick. The substrate electronic density was fixed at its theoretical value, while the density of the two upper layers was varied in order to improve the simulation. The thickness of the topmost layer coincides with the value obtained from the diffraction spectrum of Fig. 3. Such a circumstance indicates that the topmost layer in the reflectivity measurements agrees with the BZO film (7 u.c. thick). The intermediate layer (1.8 nm thick) must be associated with a defective layer at the top on the NGO substrate. Combining results from x-ray diffraction and reflectivity, the final scenario emerging is that elastic strain at the interface does not occur: elemental interdiffusion and structural defects accommodate, over an interface nanometric layer, the large difference in the lattice parameters between substrate and film. Such a defective layer extends for about four crystallographic unit cells within the substrate and about for the same extent in the BZO film. X-ray measurements are generally not sensitive to the specific element but rather to the overall electronic density. Therefore they do not allow unambiguous discrimination among different possible mechanisms. It is likely that Ga-Zr interdiffusion, Ba, and oxygen defects play the crucial role for strain relaxation.

Successively, we have investigated by SXRD the crystallographic in-plane order of the interface region where strain relaxation took place. In Figs. 5(a) and 5(b) we report intensity diffraction scans along reciprocal space H direction in the proximity of the (200) and (400) points in the reciprocal space. The full red lines in (a) and (b) represent the theoretical simulation of the diffraction curves calculated according to the interface relaxation model shown in Fig. 2. The model takes into account the disordered network of MDs. The degree of disorder has been assumed to be the same as that shown in the inset of Fig. 1. It can be noticed that the dislocation network, even if disordered as shown by the HRTEM image of Fig. 1, gives rise to quite sharp extra diffraction peaks, almost equally spaced, between the peak corresponding to the substrate and that corresponding to the BZO film. The relative peak intensities depend mostly on the extent of the defective interface region compared with the extent of the relaxed film. The width of the diffraction peaks is related with the degree of disorder in the network of MDs.

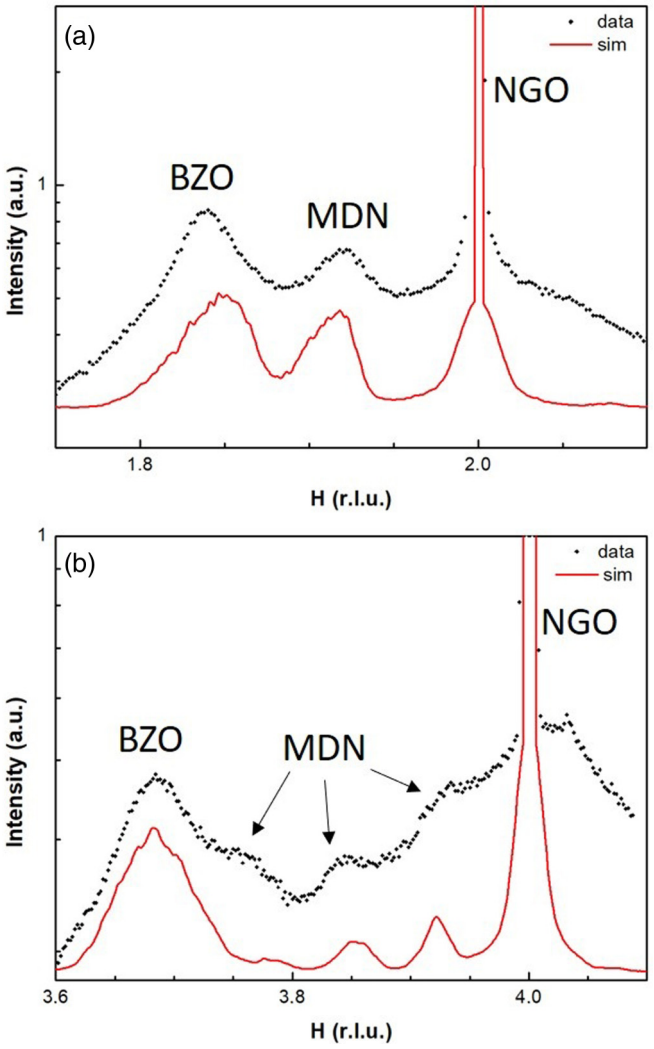

FIG. 5. Surface x-ray diffraction intensity scans along the H direction around the (200), panel (a), and (400), panel (b), points in the reciprocal lattice of a 2.9-nm BZO thick film. The full red lines represent theoretical simulations of the diffraction experimental data using the interface model shown in Fig. 2. BZO, NGO, and MDN tags specify the diffraction peaks associated to the film, to the substrate, and to the misfit dislocation network, respectively.

For the present simulation, the extent of the interface region was assumed to be 4 u.c. in the substrate plus 4 u.c. in the film, and the lattice parameter was assumed to vary linearly in this region. The overall thickness of the film was 7 u.c., in agreement with the results from the reflectivity measurements. Both the (200) and (400) scans were simulated using the same values for the structural parameters. The Supplemental Material [20] gives further details about the simulation model. Results from the simulation are in overall agreement with the experimental behavior regarding the width, position, and relative peak intensity supporting the model of the interface as described above.

In Fig. 6(a) the EIS curves are shown for three films of different thicknesses in wet H_2 atmosphere at 650 °C. A sketch of the EIS measurements arrangement is shown in Fig. 3 of the Supplemental Material [20]. Film thicknesses were 10, 100, and 500 nm, respectively. Moreover, conductivity data for a 100-nm-thick film of BZO grown on a matching substrate of MgO are added for comparison in order to exclude a major contribution to the conductivity from the surface. It can be noticed that, despite the large difference in film thickness (up to a factor 50), variations in the real part of impedance are limited to a factor less than 1.5. Such a circumstance leads us to conclude that the effective thickness of the conducting layer is the same for all three investigated samples and that it does not coincide with the whole thickness of the film. Most likely, small and uncontrolled differences in film growth conditions give rise to the measured residual small spread of the impedance values. Based on the structural analysis, we assume that electrical conduction could be confined to the defective interface layer where structural relaxation occurs. Panel (b) of Fig. 6 shows the Arrhenius plot of the conductivity behavior. The conductivity was calculated using the resistive part of the impedances while assuming the same thickness of 3 nm (according to evidence from the structural measurements) for all films. The dashed line represents the Arrhenius fit of the whole set of data. The activation energy from the Arrhenius fit is about 0.86 eV. Such a value is larger than the value currently quoted for bulk Y-doped BZO (about 0.5 eV), but it is similar to the activation energy of the blocking grain boundaries in this system [30]. In the inset of Fig. 6(b), it is shown that wet H_2 atmosphere strongly enhances the film conductance relative to a dry Ar atmosphere. According to Fig. 6, conductivity values at 650 °C are comprised between 0.37 and 0.5 S/cm.

$NdGaO_3$ and $BaZrO_3$ are both wide-band semiconducting oxides with an electronic band gap between 3 and 4 eV [31,32]. Therefore, because of the large band gap, cation vacancies or aliovalent cation substitution are expected to be compensated by oxygen vacancies rather than by electrons/holes in the conduction/valence band. Although we do not support direct measurements of the electric contribution to the overall transport mechanism, all our experimental results are consistent with a negligible electron/hole contribution of the transport properties. At the same time, stoichiometric $NdGaO_3$ and $BaZrO_3$ are not expected to show an ionic contribution to conductivity. However, Y-doped $BaZrO_3$ [33] and A-B site–doped $NdGaO_3$ [34] are excellent proton and ionic conductors, respectively. In both cases, doping induces compensating oxygen vacancies in the perovskite structure that are crucial for the proton/ionic conduction mechanisms. In the present case, XRR indicates that a sizeable amount of defects (such as cations intermixing and cation/anion vacancies) are generated in the thin layer at the interface where the strong epitaxial strain relaxes. Such a defective layer can support proton conductivity with the activation energy typical of BZY grain boundaries but a higher carrier concentration. Considering the Einstein relation and using the value of the planar prefactor D_0 from first-principles molecular dynamic (FPMD) simulations calculated for BZO film [35] and the experimental value of the activation energy for the proton conduction process E_a equal to 0.86 eV, we can obtain a rough estimate of the proton carrier density of $n \sim 10^{15}\,\mathrm{cm}^{-3}$. Overall, this would result in the large protonic conductivity at moderate temperatures shown by EIS measurements.

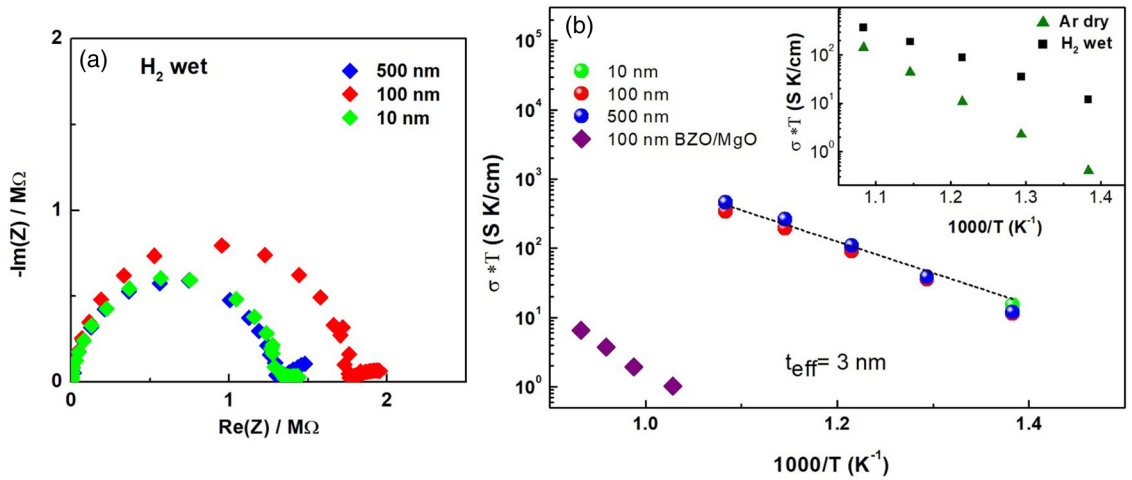

FIG. 6. (a) Electrochemical impedance spectroscopy curves obtained for three films with different thicknesses (10, 100, and 500 nm) in wet H_2 atmosphere at 650 °C. (b) Arrhenius plot of conductivity values calculated for the three films of BZO grown on NGO and for a 100-nm-thick film of BZO grown on MgO. The value of conductivity is calculated assuming the same thickness of 3 nm (according to the Fig. 2) for all the data. The dashed line represents the Arrhenius fitting of the dataset referring to films grown on NGO substrate. The activation energy from the fit is about 0.86 eV. In the inset of panel (b), conductivity measurement of 100-nm-thick BZO film in dry Ar and wet H_2 atmosphere, respectively. The comparison demonstrates the proton contribution to the conductivity.

IV. CONCLUSIONS

HRTEM and x-ray diffraction and reflectivity measurements have allowed us to disclose the nature of the interface between the strongly mismatched perovskites NGO and BZO. A quite disordered network of misfit dislocations, assisted by elemental mixing and other point defects, accommodates the large lattice mismatch (about 9%) between the film and substrate in a nanometric layer. Such a highly defective interface region extends over about 4 u.c., both in the substrate and in the film. No elastic distortion occurs at this interface. This disordered region has a strong influence on the transport properties of the film. It creates an abundance of vacancies which, when filled with hydroxyl ions, increase the ion carrier concentration density. The enhancement of film conductance in wet H_2 relative to a dry Ar or dry air atmosphere supports the proton nature of conductivity in these samples. Moreover, assuming that charge transport occurs in the highly defective interface region (about 3 nm thick), a conductivity value equal to about 5×10^{-1} S/cm at 650 °C in wet atmosphere is estimated. The presence of dislocations, which act similarly to grain boundaries, enhance the activation energy of the transport mechanism. The high value of the activation energy in the Arrhenius plot (0.86 eV) is consistent with previous grain-boundary conduction measurements in the BZO system. These results suggest that epitaxial superlattices based on highly mismatched oxides, having individual layers a few unit cells thick, can show strongly enhanced ionic/proton conduction. Our experimental results and the qualitative explanation proposed are related to the in-plane conductivity. Conventional fuel-cell devices consist of a cathode and anode on the opposite surfaces of an electrolyte membrane, where the transport is transverse with respect to the surface. In the actual system we discussed here, in order to take advantage of the high conductivity values, a planar device fabrication technology is required. The properties of these defective interfaces could be useful to fabricate novel dual miniaturized in-plane solid oxide fuel cells using state-of-the-art microfluidic and microelectromechanical technology [36].

[1] J. Mannhart and D. G. Schlom, Science **327**, 1607 (2010).
[2] A. Ohtomo and H. Y. Hwang, Nature (London) **427**, 423 (2004).
[3] N. Reyren, S. Thiel, A. D. Caviglia, L. F. Kourkoutis, G. Hammerl, C. Richter, C. W. Schneider, T. Kopp, A.-S. Ruetschi, and D. Jaccard, Science **317**, 1196 (2007).
[4] D. Di Castro, M. Salvato, A. Tebano, D. Innocenti, C. Aruta, W. Prellier, O. I. Lebedev, I. Ottaviani, N. B. Brookes, M. Minola, M. Moretti Sala, C. Mazzoli, P. G. Medaglia, G. Ghiringhelli, L. Braicovich, M. Cirillo, and G. Balestrino, Phys. Rev. B **86**, 134524 (2012).
[5] D. Di Castro, C. Cantoni, F. Ridolfi, C. Aruta, A. Tebano, N. Yang, and G. Balestrino, Phys. Rev. Lett. **115**, 147001 (2015).
[6] A. Tebano, C. Aruta, S. Sanna, P. G. Medaglia, G. Balestrino, A. A. Sidorenko, R. De Renzi, G. Ghiringhelli, L. Braicovich, V. Bisogni, and N. B. Brooks, Phys. Rev. Lett. **100**, 137401 (2008).
[7] D. Pergolesi, V. Roddatis, E. Fabbri, C. W. Schneider, T. Lippert, E. Traversa, and J. A. Kilner, Sci. Technol. Adv. Mater. **16**, 015001 (2015).
[8] P. P. Dholabhai, G. Pilania, J. A. Aguiar, A. Misra, and B. P. Uberuaga, Nat. Commun. **5**, 5043 (2014).
[9] C. Leon, J. Santamaria, and B. A. Boukamp, MRS Bull. **38**, 1056 (2013).
[10] J. Garcia-Barriocanal, A. Rivera-Calzada, M. Varela, Z. Sefrioui, E. Iborra, C. Leon, S. J. Pennycook, and J. Santamaria, Science **321**, 676 (2008).
[11] X. Guo and J. Maier, Adv. Mater. **21**, 2619 (2009).

[12] N. Sata, K. Eberman, K. Eberl, and J. Maier, Nature (London) **408**, 946 (2000).
[13] C. Korte, A. Peters, J. Janek, D. Hesse, and N. Zakharov, Phys. Chem. Chem. Phys. **10**, 4623 (2008).
[14] A. Peters, C. Korte, D. Hesse, N. Zakharov, and J. Janek, Solid State Ionics **178**, 67 (2007).
[15] S. Sanna, V. Esposito, A. Tebano, S. Licoccia, E. Traversa, and G. Balestrino, Small **6**, 1863 (2010).
[16] V. Foglietti, N. Yang, A. Tebano, C. Aruta, E. Di Bartolomeo, S. Licoccia, C. Cantoni, and G. Balestrino, Appl. Phys. Lett. **104**, 81612 (2014).
[17] N. Yang, C. Cantoni, V. Foglietti, A. Tebano, A. Belianinov, E. Strelcov, S. Jesse, D. Di Castro, E. Di Bartolomeo, and S. Licoccia, Nano Lett. **15**, 2343 (2015).
[18] R. Felici, C. Aruta, N. Yang, F. Zarotti, V. Foglietti, C. Cantoni, A. Tebano, F. Carlà, and G. Balestrino, Phys. Status Solidi B **256**, 1800217 (2019).
[19] S. W. Saeed, T. Norby, and T. S. Bjørheim. J. Phys. Chem. C **123**, 20808 (2019).
[20] See Supplemental Material at http://link.aps.org/supplemental/10.1103/PhysRevMaterials.3.103606 for the description of the crystallographic structure, parameters of XRR fit, additional details of the diffraction simulation model, and EIS measurements sketch.
[21] R. S. Roth, J. Res. Nat. Bur. Stand. **58**, 75 (1957).
[22] S. Geller, Acta Cryst. **10**, 243 (1957).
[23] O. Balmes, R. van Rijn, D. Wermeille, A. Resta, L. Petit, H. Isern, T. Dufrane, and R. Felici, Catal. Today **145**, 220 (2009).
[24] S. Roobol, W. Onderwaater, J. Drnec, R. Felici, and J. Frenken, J. Appl. Crystallogr. **48**, 1324 (2015).
[25] https://www.synchrotron-soleil.fr/en/beamlines/sixs
[26] http://www.kaminski.up.lublin.pl/WinRod.html
[27] E. Vlieg, J. Appl. Crystallogr. **33**, 401 (2000).
[28] A. Lasia, Electrochemical Impedance Spectroscopy and its Applications, in *Modern Aspects of Electrochemistry*, edited by B. E. Conway, J. O. Bockris, and R. E. White, Vol. 32 (Springer, Boston, MA, 2002).
[29] I. K. Robinson and D. J. Tweet, Reports Prog. Phys. **55**, 599 (1992).
[30] M. Shirpour, B. Rahmati, W. Sigle, P. A. van Aken, R. Merkle, and J. Maier, J. Phys. Chem. C **116**, 2453 (2012).
[31] R. Terki, H. Feraoun, G. Bertrand, and H. Aourag, Phys. Status Solidi **242**, 1054 (2005).
[32] A. Dahani, H. Alamri, B. Merabet, A. Zaoui, S. Kacimi, A. Boukortt, and M. Bejar, Chin. Phys. B **26**, 17101 (2017).
[33] N. Bonanos, Solid State Ionics **53**, 967 (1992).
[34] D. Lybye, F. W. Poulsen, and M. Mogensen, Solid State Ionics **128**, 91 (2000).
[35] A. Fluri, A. Marcolongo, V. Roddatis, A. Wokaun, D. Pergolesi, N. Marzari, and T. Lippert, Adv. Sci. **4**, 1700467 (2017).
[36] M. Kuhn and T. W. Napporn, Energies **3**, 57 (2010).